





Article

A First-Principles Study on the Multilayer Graphene Nanosheets Anode Performance for Boron-Ion Battery

Mustapha Umar ¹, Chidera C. Nnadike ¹, Muhammad Haroon ¹, Ismail Abdulazeez ^{2,*}, Khalid Alhooshani ^{1,3}, Abdulaziz A. Al-Saadi ^{1,3} and Qing Peng ^{4,5,6,*}

- ¹ Chemistry Department, King Fahd University of Petroleum and Minerals, Dhahran 31261, Saudi Arabia; g201708770@kfupm.edu.sa (M.U.); g201707330@kfupm.edu.sa (C.C.N.); muhammad.hanif@kfupm.edu.sa (M.H.); hooshani@kfupm.edu.sa (K.A.); asaadi@kfupm.edu.sa (A.A.A.-S.)
- ² Interdisciplinary Research Center for Membranes and Water Security, King Fahd University of Petroleum and Minerals, Dhahran 31261, Saudi Arabia
- ³ Interdisciplinary Research Center for Refining and Advanced Chemicals, King Fahd University of Petroleum and Minerals, Dhahran 31261, Saudi Arabia
- ⁴ Interdisciplinary Research Center for Hydrogen and Energy Storage, King Fahd University of Petroleum and Minerals, Dhahran 31261, Saudi Arabia
- ⁵ Physics Department, King Fahd University of Petroleum and Minerals, Dhahran 31261, Saudi Arabia
- ⁶ KACARE Energy Research and Innovation Center at Dhahran, Dhahran 31261, Saudi Arabia
- * Correspondence: ismail.abdulazeez@kfupm.edu.sa (I.A.); qing.peng@kfupm.edu.sa (Q.P.)

Abstract: Advanced battery materials are urgently desirable to meet the rapidly growing demand for portable electronics and power. The development of a high-energy-density anode is essential for the practical application of B³⁺ batteries as an alternative to Li-ion batteries. Herein, we have investigated the performance of B³⁺ on monolayer (MG), bilayer (BG), trilayer (TG), and tetralayer (TTG) graphene sheets using first-principles calculations. The findings reveal significant stabilization of the HOMO and the LUMO frontier orbitals of the graphene sheets upon adsorption of B³⁺ by shifting the energies from −5.085 and −2.242 eV in MG to −20.08 and −19.84 eV in 2B³⁺@TTG. Similarly, increasing the layers to tetralayer graphitic carbon B³⁺@TTG_asym and B³⁺@TTG_sym produced the most favorable and deeper van der Waals interactions. The cell voltages obtained were considerably enhanced, and B³⁺/B@TTG showed the highest cell voltage of 16.5 V. Our results suggest a novel avenue to engineer graphene anode performance by increasing the number of graphene layers.

Keywords: DFT; graphene layers; boron-ion battery; adsorption; reduced density gradient



Citation: Umar, M.; Nnadike, C.C.; Haroon, M.; Abdulazeez, I.; Alhooshani, K.; Al-Saadi, A.A.; Peng, Q. A First-Principles Study on the Multilayer Graphene Nanosheets Anode Performance for Boron-Ion Battery. *Nanomaterials* **2022**, *12*, 1280. <https://doi.org/10.3390/nano12081280>

Academic Editors: Jin-Hae Chang and Marcelo Antunes

Received: 9 March 2022

Accepted: 6 April 2022

Published: 9 April 2022

Publisher's Note: MDPI stays neutral with regard to jurisdictional claims in published maps and institutional affiliations.



Copyright: © 2022 by the authors. Licensee MDPI, Basel, Switzerland. This article is an open access article distributed under the terms and conditions of the Creative Commons Attribution (CC BY) license (<https://creativecommons.org/licenses/by/4.0/>).

1. Introduction

The past two decades have witnessed impressive improvements in lithium-ion battery (LIB) technologies for portable consumer electronics, electrical devices, and energy storage [1,2]. LIBs have demonstrated outstanding performance, including superior energy density, operating voltage, life cycle, and minimal rate of self-discharge, as well as low volume [3]. Generally, LIBs have exhibited exceptional performance over other known rechargeable ion battery systems [4–6]. More significantly, the 2019 Nobel Prize award in Chemistry was received by researchers in the field of lithium-ion batteries [7,8]. Despite the appealing applicability of LIBs, limitations such as narrow lifetime, inadequate performance at low temperatures, and most severely, the swift exhaustion of the lithium mineral reserves, may represent a setback for LIB technology. For example, around one-quarter of the global Li precursor materials are utilized to produce LIBs, thereby delivering a strong hike in the price of lithium carbonate [9–11]. On this premise, a wide range of research has been dedicated to alternative elements for ion battery technology [2,8,12–14]. Among many candidates, sodium-ion batteries (SIBs) are expected to substitute the LIBs due to their low cost, non-toxicity, and nearly limitless sodium mineral reserve [15,16]. Moreover, sodium possesses similar chemical properties as lithium since they belong to the same alkali metal

group. The replacement of lithium with sodium could take advantage of the existing and mature technologies and product lines with only minimal modifications. Unfortunately, SIBs suffer from low energy storage capacity and energy density, and a low rate of charging and discharging [17].

The developmental process of ion batteries in the past few decades has advanced since the discovery of nanotechnology and nanomaterials, which provide excellently performing electrodes [18–22]. Nanostructures such as graphenylene, nanotubes, nanoeeggs, nanocones, fullerene, and graphene have been studied for nano-electrode applications [23–25]. For instance, a report from Youn et al. [8] showed that graphene nanomaterials have excellent ion battery electrode properties [26]. Particularly, structural modifications such as doping with foreign materials and/or chemical functionalization of electrode nanostructures have been reported to enhance the performance of these nanomaterials [1,27–29]. , reported that boron nitride nanosheets (BNNS) have improved anodic voltage capacity when functionalized with conducting polymers such as polypyrrole [1]. Furthermore, Hardikar et al. (2014) [28] and Qie et al. [30] reported improved performance of LIB through the replacement of graphene's carbon atoms with boron or nitrogen. Similarly, in 2013, Yu [31] reported that the performance of LIB anodic materials can be significantly improved by defective nitrogen-doping of graphene sheets. Yu established that N-substituted graphene possessing double vacancies is mostly likely to significantly enhance the performance of LIBs. Experimentally, Chen et al [32] studied the effect of N-doping of hard carbon for robust anodic material application for high-performance potassium-ion batteries (PIBs). Their report showed a high-capacity rate of 154 mAh/g at 72 cycles and a long-lasting life cycle of 4×10^3 with efficient rate capability. Similar improved electrode properties, such as enhanced conductivity and voltage capacities via carbon anode N/S-codoped hierarchy for SIBs, have also been reported [33]. Commonly, less compact elements such as boron and nitrogen can yield suitable adsorption sites for ions that show weak interaction with the pristine graphene.

Graphene is a 2D nanosheet comprising sp^2 -hybridized carbon atoms. The sp^2 -hybridized bonds offer excellent structural reliability and outstanding mechanical properties, which are important for anodic material applications [34–49]. Its honeycomb extended network represents the fundamental block structure for other crucial allotropes such as stacked 3D graphite, rolled form 1D nanotubes, and the wrapped form 0D fullerenes [50]. Graphene has been extensively investigated as an anodic material [51–54] owing to its properties such as superior surface area and promising electronic properties [30]. More specifically, one-dimensional nanotubes and zero-dimensional fullerenes have been utilized as anodic materials in LIBs and have demonstrated increased electrochemical performance [51,55,56]. However, these carbon-based materials only exhibit short-lived enhanced performance when compared with 3D graphite. It is already established that the performance of nanomaterials extensively relies on their morphologies and structures. Hence, graphene nanosheets would most likely provide improved electrochemical activities. Using first-principle simulations, Gerouki et al. reported that graphene sheets of ca. 0.7 nm thick offer the best storage density with Li_4C_6 [57], while Hardikar et al. reported the electrochemical performance of LIBs with graphene sheets of four layers and a large specific surface area of $492.5 \text{ m}^2/\text{g}$ [30]. Lian et al. obtained an excellent specific capacity of about 900–1264 mAh/g for more than four layers of high-quality graphene sheets [51]. Furthermore, doping graphene support(s) with boron atom(s)/ion(s) demonstrated an improvement in the anodic performance of the support materials and, consequently, the cell voltages [58]. It has conferred on the support materials high electronic mobility, indicating potential to attain an excellent rate of performance.

Despite these efforts, there are limited reports on the intercalation of elements such as boron within the layers of high-quality graphene nanosheets for improved anodic boron-ion batteries (BIBs). Hence, in the present study, we report a theoretical investigation of the anodic performance of graphene nanosheets for boron-ion batteries. Previous reports [30,51,57] have shown that multilayer graphene with fewer layers demonstrates

superior electrochemical performance for ion battery anodic applications. Therefore, we investigated the electrochemical performance of single-layer to four-layer graphene sheets. With this investigation, we aim to pave the way for the successful design of extremely effective materials for energy storage.

2. Theoretical Methods

All structural optimizations and electronic properties calculations were performed employing Density Functional Theory (DFT) as implemented on Gaussian 09 suite. The Perdew–Burke–Ernzerhof (PBE) functional belonging to the generalized gradient approximation (GGA) functional was used to account for the exchange–correlation energy because it provides reasonable accuracy without prolonged computational times, while the 6–311 G(d,p) basis set was adopted [8,59–61]. The PBE is an effective standardized functional because, by design, each component adheres to some exact conditions [62]. It follows the spin-scaling relationship exactly and reclaims the linear response of the LDA for a small-scale gradient [63]. The PBE functional is a full ab initio functional which relies on μ , β , K , and γ parametric values fixed from theoretical factors. Similarly, the 6–311 G(d,p) basis set was adopted because it provided a reliable assessment of the energies of solvation when employing an implicit solvent standard/prototype when compared to other highly revered basis sets [64]. The influence of dispersion-corrected functionals on the geometry of the layers was similarly examined using Grimme’s D3 approach [65–68]. Typically, all atoms were set free in the single- and double-layer slab. The resulting layers slab models are shown in Figure 1. However, to stabilize the computed surface energies for the three and four layers, the atoms were frozen. Studies have shown that freezing layers does not affect surface energies [59]. The adsorption energies (E_{ad}) were calculated according to the following equation [69]:

$$E_{ad} = E_{Complex} - (E_{adsorbate} + E_{substrate}) \quad (1)$$

where $E_{complex}$, $E_{adsorbate}$, and $E_{substrate}$ represent the energies of the adsorbate and boron ion(s), graphitic layer(s), and the substrate, respectively. Likewise, the final cell voltages (V_{cell}) were calculated utilizing the Nernst equation:

$$V_{cell} = \frac{-\Delta G_{cell}}{zF} \quad (2)$$

where zF represents the charge on the metal ions and Faraday constant, and ΔG_{cell} stands for the Gibbs free energy of the overall cell reactions as

$$\Delta G_{cell} = \Delta E_{cell} + P\Delta V - T\Delta S \quad (3)$$

where ΔG corresponds to the change in the internal energies of the cell, because the influences of entropy and the volume effects are insignificant (<0.01 V) to the cell voltage (V_{cell}) [1]. We investigated the effect of the number of layers and boron ions on the cell voltage. Our model of the systems with pristine layered graphene sheets is illustrated in Figure 1. The models of the boron-intercalated layered graphene sheets are shown in Figure 2. The GaussSum program was used to depict the density of states (DOS) plot [70].

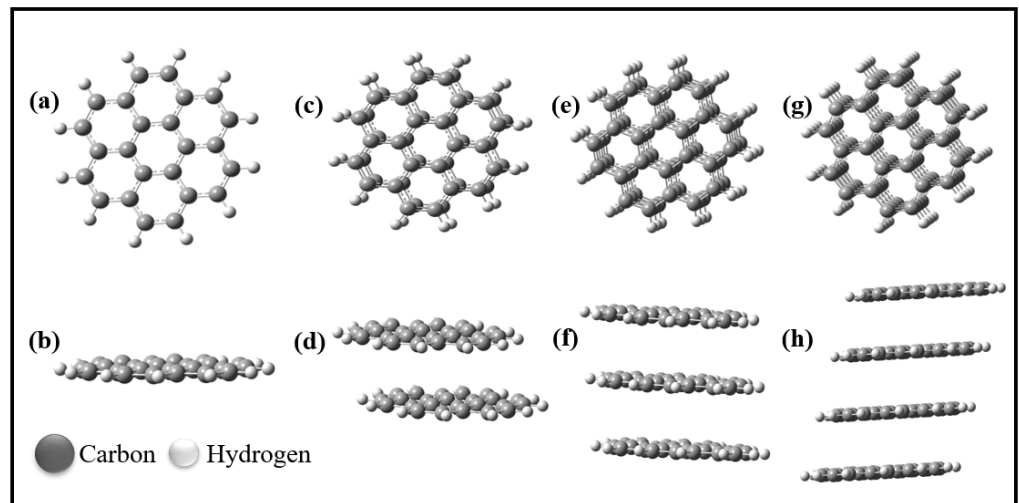


Figure 1. Optimized structures of (a,b) monolayer graphene sheet (MG), (c,d) bilayer graphene sheet (BG), (e,f) trilayer graphene sheet (TG), and (g,h) tetralayer graphene sheet (TTG). (b,d,f,h) Side-view orientation of the graphene sheets.

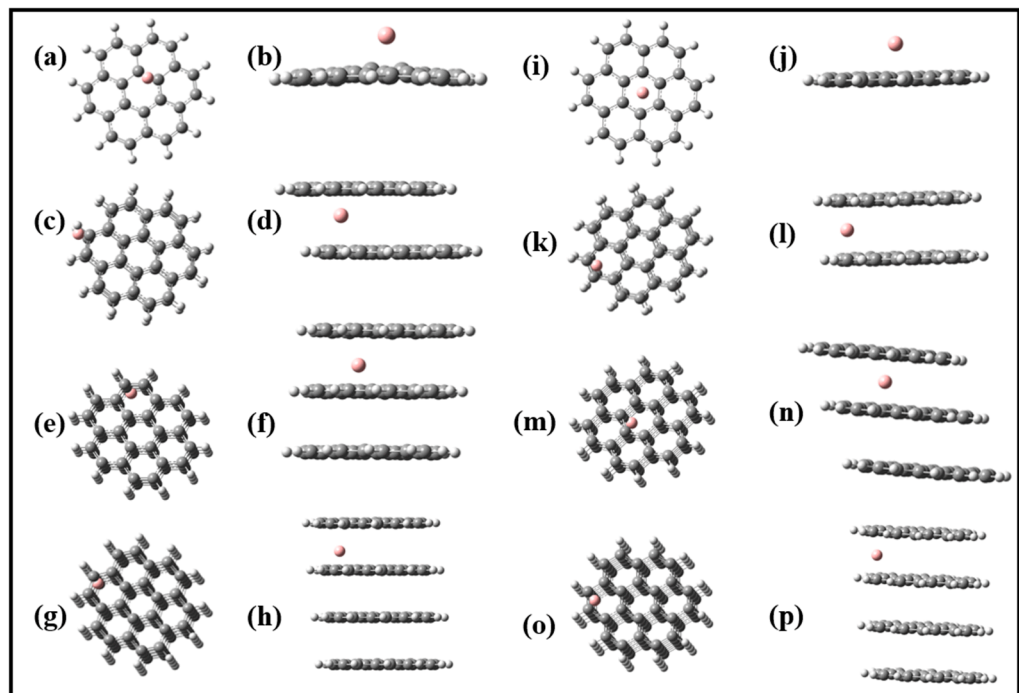


Figure 2. Optimized structures of (a,b) B@MG (side and top views), (c,d) B@BG (side and top views), (e,f) B@TG (side and top views), (g,h) B@TTG (side and top views), (i,j) B³⁺@MG (side and top views), (k,l) B³⁺@BG (side and top views), (m,n) B³⁺@TG (side and top views), and (o,p) B³⁺@TTG (side and top views).

3. Results and Discussion

3.1. Structural Properties

Pristine graphene nanosheets: The optimized electronic structures of the graphene sheet and the different multilayer orientations of the sheets are shown in Figure 1. In the multilayer orientations, the graphene sheets were differently oriented: AB and AA for bilayer; ABA and AAB for trilayer; and ABAB, AABB, and AABA for tetralayer before optimization. However, after optimization, it was observed that the layers favored AA orientation in all the arrangements, as similarly observed by other reports [8].

Boron-intercalated and boron-free graphene nanosheets: Figure 2 shows the optimized structures of the boron atom and its corresponding ion (B^{3+}) adsorbed on the monolayer graphene sheets (MG) (Figure 2a,b,i,j). The boron species preferred a central position on the MG after optimization even after being positioned at different points on the sheets before optimization. In the multilayered graphene orientations, the intercalated B or B^{3+} preferred the edges of the multilayer sheets after optimization. The reduced density gradient (RDG) maps for the complexes imply weak van der Waals interactions predominantly among the boron species and the graphene sheets. It may offer explanations for the preferred arrangements of the complexes. As shown in Figure S1 in the Supplementary Materials, the TG and TTG have two boron atoms and/or ions (B^{3+}) alternatively intercalated within two layers of the graphene sheets.

We examined the distances between the layers of the graphene (α -layer and β -layer) and the boron species (B/ B^{3+}). As shown in Figure 3, the red bars represent the distance or degree of compactness between the β -layer and the boron species. Similarly, the green bars represent the degree of compactness between the α -layer and the boron species (B/ B^{3+}). The monolayer graphene arrangement results from the " α -layer"-B/ B^{3+} arrangement with the subsequent multilayer arrangements resulting from the successive addition of two or more graphene layers in the α - and/or β -layered direction(s). The " α -layer"-B/ B^{3+} distances (the green bars) are generally shorter than the " β -layer"-B/ B^{3+} distances (the red bars), probably due to stronger interaction between the α -layer and the boron species before the subsequent addition of the β -layer(s) to generate the multilayers. The β -layer distances from the boron atoms (B) are also longer than their corresponding distances from the ionic boron species (B^{3+}), which further amplifies the ionic interaction effect of the boron with the graphene layer(s).

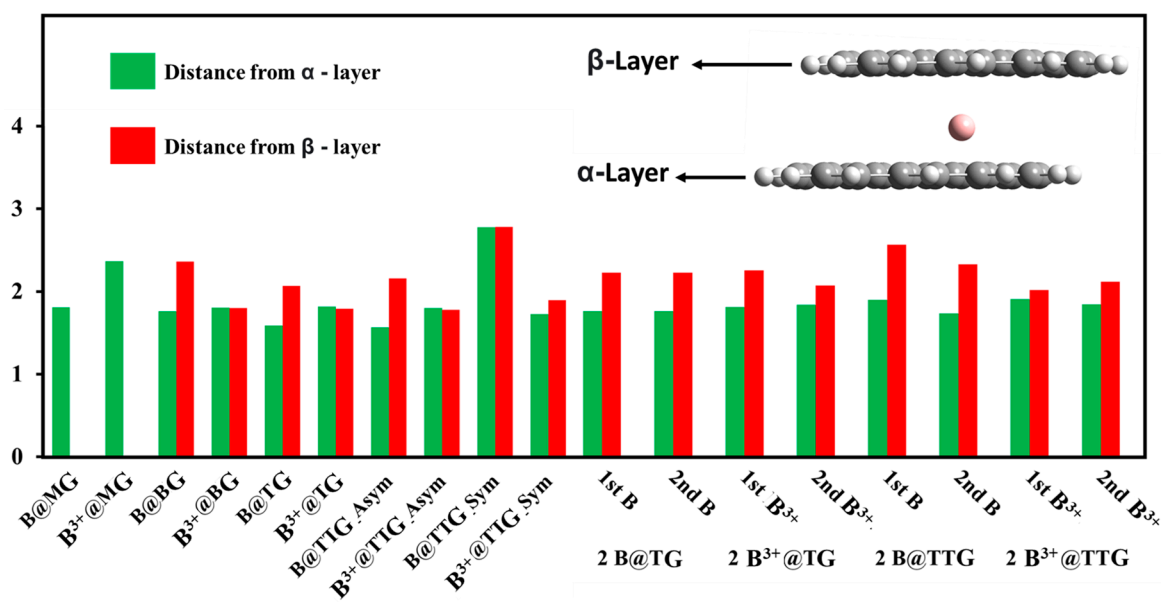


Figure 3. The distance between the graphene layers (α -layer and β -layer) and the boron species (B and/or B^{3+}). The green bars represent the " α -layer"-B/ B^{3+} distance while the red bars represent the " β -layer"-B/ B^{3+} distance.

In the cases of arrangements having more than one boron atom/ion, similarly, distance trends and effects are pertinent. Generally, the presence of the boron atoms/ions intercalation influences the degree of compactness of the graphene layer arrangement; however, this may likely be insignificant to the progressive drifting of the boron atoms and/ions during the charging and discharging process of the ion battery, as illustrated in the RDG surface analysis.

3.2. Electronic Properties of Graphene Sheets and Adsorbed B^{3+} on the Graphene Sheets

The energies of HOMO, LUMO, and HOMO–LUMO bandgap of the graphene sheets and the intercalated B^{3+} ions are calculated in Figure 4a–g and Figures S2–S5 in the Supplementary Materials. The presence of higher HOMO energy is a characteristic associated with donating tendencies, while low LUMO energy is considered as accepting ability.

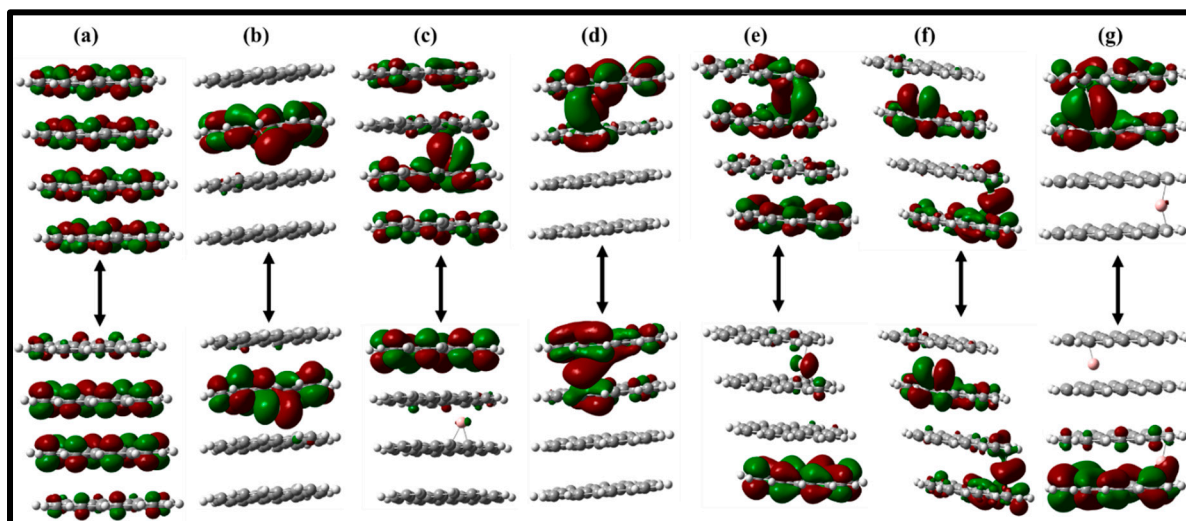


Figure 4. Molecular orbital HOMO (Lower) and LUMO (upper) of (a) tetralayer graphene sheet (TTG), (b) B@TTG-sym, (c) B^{3+} @TTG-sym, (d) B@TTG-asm, (e) B^{3+} @TTG-asm, (f) 2B@TG (side and top views), and (g) 2 B^{3+} @TTG (side and top views).

The HOMO energies (Table S1 in Supplementary Materials) of the graphitic layers relatively decrease from monolayer to tetralayer, whereas the LUMO energies recorded no significant changes. This suggests that the HOMO and LUMO levels of graphene sheets were significantly stabilized by the adsorption of the B^{3+} ion. The HOMO and LUMO levels shift from -5.085 and -2.242 eV in MG to -20.08 and -19.84 eV in $2B^{3+}$ @TTG. Although there are no significant differences between the energies of the HOMO and LUMO of the singly adsorbed B^{3+} ions, relative variations are seen with doubly adsorbed B^{3+} ions: -20.08 and -19.84 eV for $2B^{3+}$ @TG and -18.33 and -17.66 eV, corresponding to $2B^{3+}$ @TTG, which can be attributed to the addition of B^{3+} into the graphene sheets. Accordingly, upon adsorption of B^{3+} , the global electronic energy bandgap (E_g) of the graphene sheets is reduced significantly to about 99.89%, and the same trend is observed with adsorbed neutral boron (Table S1 in Supplementary Materials).

The observed order with adsorbed neutral boron could be due to the existence of unpaired electrons in the valence shell of the neutral boron; the HOMO level of the graphitic layer is largely impacted by altering to higher energies, suggesting a considerable destabilization [71]. Similarly, the E_g of the doubly adsorbed B^{3+} increases in comparison with the singly adsorbed B^{3+} , which could be attributed to the decreased LUMO level and increased HOMO level. In electrostatic potential maps (ESPs), colors are used as indicators for different electrostatic potential values: blue demonstrates high positive (electron-deficient) regions of the species, while green displays the region of zero potential [72]. As illustrated in Figures S6 and S7, the ESPs of the B^{3+} form of B^{3+} @MG, B^{3+} @BG, B^{3+} @TG, B^{3+} @TTG_asm, B^{3+} @TTG_sym, $2B^{3+}$ @TG, and $2B^{3+}$ @TTG reveal predominantly more electropositive regions (blue color). This is more severe with B^{3+} @MG, B^{3+} @BG, $2B^{3+}$ @TG, and $2B^{3+}$ @TTG configurations. However, with the addition of layers, a slightly neutral region with B^{3+} @TG, B^{3+} @TTG_asm, and B^{3+} @TTG_sym was observed.

3.3. Adsorption of B^{3+} Ions on the Wall of Graphene Sheets

The adsorption of B^{3+} ions on the wall of the solid host is considered an alternative B^{3+} -storage mechanism. The model sheets studied with adsorbed B^{3+} ions are depicted in Figure 2. The role of the numbers of graphene sheets and the number of B^{3+} ions are examined. We studied the adsorption characteristics of graphitic carbon sheets by intercalating B^{3+} ions between the bilayer, trilayer, and tetralayer (Figure 2). The positions of the intercalated B^{3+} ions between the graphene sheets were selected thoroughly. All the B^{3+} ions were placed in the central plane defined by the graphene sheet and allowed to relax in all directions.

The adsorption energies (E_{ad}) for the singly intercalated B^{3+} ions were calculated as 3.987, -320.1 , -477.0 , -638.4 , and -637.6 kcal/mol for $B^{3+}@MG$, $B^{3+}@BG$, $B^{3+}@TG$, $2B^{3+}@TTG_asym$, and $B^{3+}@TTG_sym$, respectively (Figure 5). Furthermore, the tetralayer graphitic carbon $B^{3+}@TTG_asym$ and $B^{3+}@TTG_sym$ exhibited the most favorable and stable adsorption configuration of B^{3+} intercalated within different layers of graphene sheets. Similarly, the E_{ad} corresponding to the formation of $2B^{3+}@TG$ and $2B^{3+}@TTG$ configurations having double B^{3+} ion intercalations are -467.9 and -628.7 kcal/mol, respectively. Thus, the addition of an extra sheet to form $2B^{3+}@TTG$ was more energetically favored than the formation of the $2B^{3+}@TG$ with fewer layers. Meanwhile, a very weak interaction was observed on $B^{3+}@MG$ with an E_{ad} of 3.987 kcal/mol, in agreement with some research findings on Li [73].

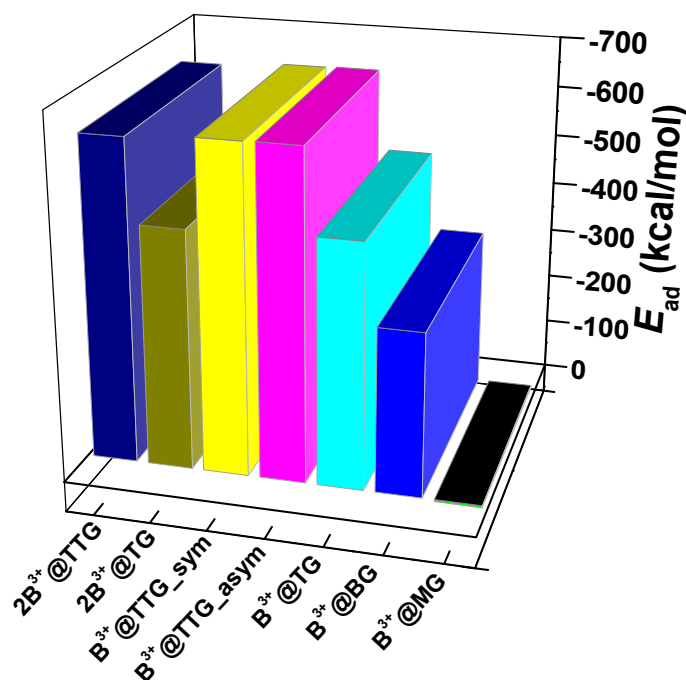


Figure 5. Adsorption energies (E_{ad}) of B^{3+} ions on the seven studied systems including $B^{3+}@MG$, $B^{3+}@BG$, $B^{3+}@TG$, $B^{3+}@TTG$ -asym, $B^{3+}@TTG$ -sym, $2B^{3+}@TG$, and $2B^{3+}@TTG$.

The reduced density gradient (RDG) isosurfaces of the interactions are shown in Figure 6 and Figure S8. Bader's theory of atoms in molecules categorized van der Waals interactions, strong steric effects, and hydrogen bond interactions to exhibit low ρ and relatively larger ρ values, respectively [74]. RDG isosurfaces plots reveal the binding interaction region and the modes [75]. The RDG isosurfaces analysis results of BC_6 and BC_2 mode of binding interactions manifest the weak van der Waals interaction between B^{3+} and graphene sheets, as displayed in Figure 6 and Figure S8, suggesting the physical nature of the reaction and high diffusion affinity of the B^{3+} ions [76]. Except for $B^{3+}@MG$, in which the intercalated B^{3+} is equidistant with six carbons of the graphene ring to form BC_6 (Figure 6a,b), all other configurations revealed the BC_2 geometry, where the B^{3+} ions

are adjacent to two carbon atoms, one above and one below the graphene layer (Figure 6c–f and Figure S8).

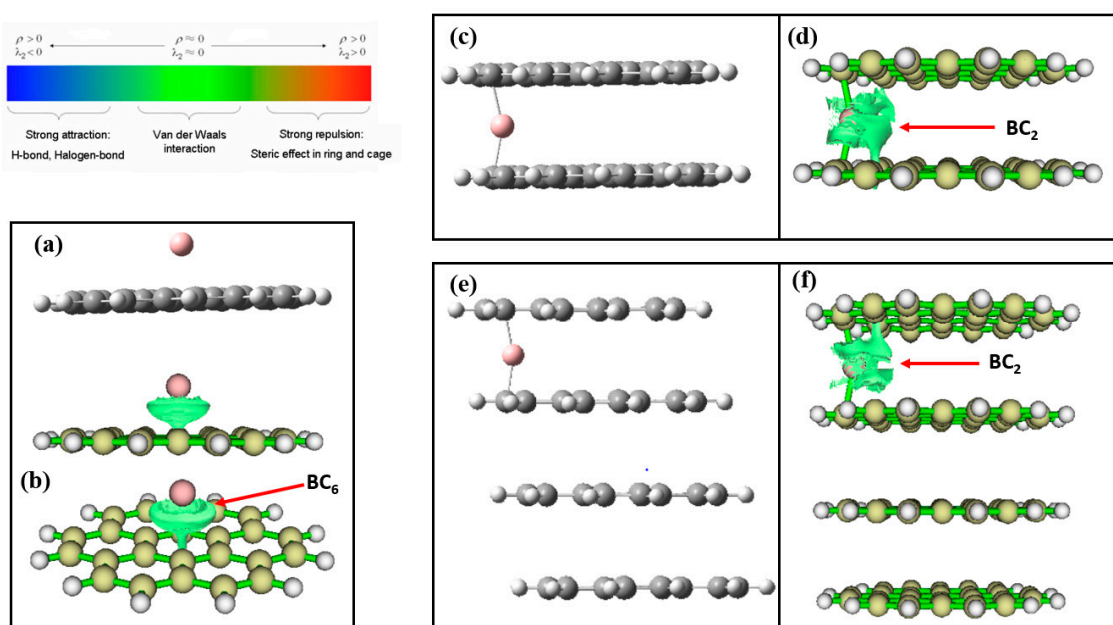


Figure 6. The reduced density gradient (RDG) isosurfaces analyses of (a,b) $B^{3+}@MG$ (complex and RDG), (c,d) $B^{3+}@BG$ (complex and RDG), (e,f) $B^{3+}@TTG$ (complex and RDG). Blue regions correspond to strong hydrogen bonds; red regions indicate strong steric effects; green regions describe strong van der Waals interactions.

To gain in-depth knowledge of the interactions between the intercalated B^{3+}/B atom and the numbers of graphene sheets, we calculated the density of states (DOS) and the projected density of states (PDOS) of the B^{3+}/B atom adsorbed graphene sheets as displayed in Figure 7 and Figures S9–S12. The projected density of states (PDOS) plots revealed the reduction in E_g from 2.843 eV in MG to 2.472 eV with TTG, which is likely due to an increase in the number of graphene sheets (Figure 7). Similarly, as seen in the PDOS and the frontier molecular orbital, the number of states at the HOMO is influenced by the carbon atoms, while the contribution at the LUMO increases with an increase in the graphene sheet. In general, the valence and conduction bands of MG, BG, TG, and TTG are dominated by the p orbitals of both types of carbon atoms (either bonded with C or H). Unlike the boron atoms, the adsorption of B^{3+} significantly reduces the levels of HOMO and LUMO in the graphene sheets and limits their E_g , which would simplify the diffusion of electrons or charges. Analysis of the PDOS and frontier molecular orbital implies that the LUMO is localized on the B^{3+} while the HOMO is confined on the graphitic sheets but improved with the addition of the sheets. Furthermore, the adsorption of two B^{3+} into TG and TTG followed the same trend. However, upon adsorption of boron, a new electronic peak (indicated by the red arrow) is generated, which mainly comes from the contribution of 2p unpaired electrons of the B atom (Figures S9a–c, S10c,d and S12c,d). The presence of unpaired electrons at the HOMO generates unstable singly occupied molecular orbitals, resulting in the lowering of the HOMO from -5.085 eV in $B@MG$ to 0.040 eV in $2B@TG$ (Table S1). In general, the PDOS and the frontier molecular orbital analysis illustrate that the contribution of the number of states at the HOMO is mainly influenced by the boron atoms, while the LUMO is controlled by the atoms of the graphene sheet.

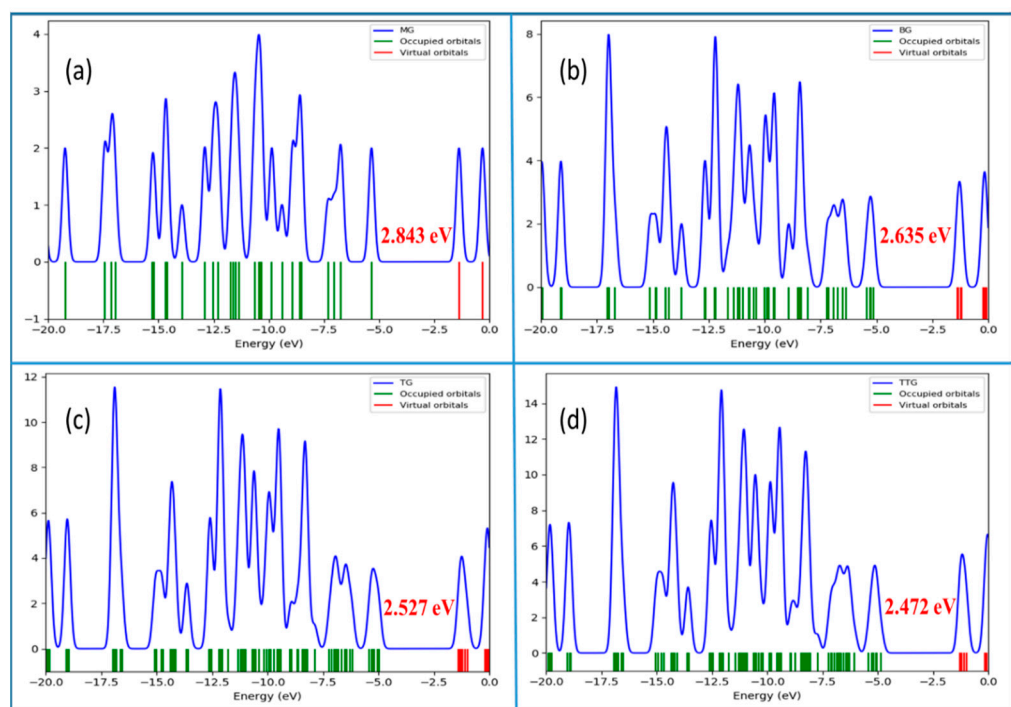


Figure 7. Partial density of states (PDOS) plots of (a) MG (b) BG, (c) TG, and (d) TTG.

Natural bond orbitals (NBO) population analysis was conducted to estimate the charge transfer in the complexes and is presented in Figures S13 and S14. As shown in Table 1, the complexes exhibit σ donation between the graphene sheets and the B^{3+} ion, and π back-donation from the B^{3+} ion to the vacant orbitals of the graphene atoms. The NBO results likewise indicate that the charge transfer is more sensitive to the sum of adsorbed B^{3+} ions in $2B^{3+}@TG$ and $2B^{3+}@TTG$ than the other complexes, suggesting greater stability in the $B^{3+}@MG$, $B^{3+}@BG$, $B^{3+}@TG$, $B^{3+}@TTG_asym$, and $B^{3+}@TTG_sym$ configurations in contrast to the $2B^{3+}@TG$ and $2B^{3+}@TTG$ complexes.

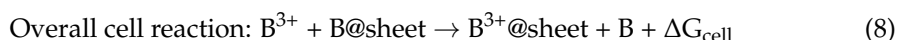
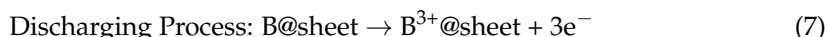
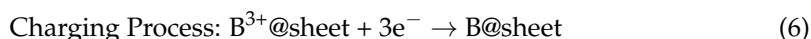
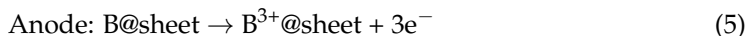
Table 1. Summary of NBO analysis of π -complexation between B^{3+} ions and the graphene sheets.

Complexes	C \rightarrow B^{3+} Interaction (σ Donation)	$B^{3+} \rightarrow$ C Interaction ($p-\pi^*$ Back-Donation)	Total Charge
$B^{3+}@MG$	0.645	-0.049	0.596
$B^{3+}@BG$	0.971	C1 = -0.413 C2 = -0.409	0.560
$B^{3+}@TG$	1.082	C1 = -0.251 C2 = -0.242	0.836
$B^{3+}@TTG_asym$	0.916	C1 = -0.443 C2 = -0.429	0.480
$B^{3+}@TTG_sym$	0.981	C1 = -0.491 C2 = -0.219	0.626
$2B^{3+}@TG$	$B^{3+}1 = 1.212$ $B^{3+}2 = 0.994$	C1 = -0.328 C2 = -0.210 C1 = -0.323 C2 = -0.237	0.630
$2B^{3+}@TTG$	$B^{3+}1 = 1.002$ $B^{3+}2 = 1.017$	C1 = -0.443 C2 = -0.400 C1 = -0.325 C2 = -0.341	0.633

C1 and C2 represent the shortest distant carbon of the graphene sheet above or below, respectively, and B^{3+} is the adsorbed boron ion, π^* represent the anti-bonding π -orbitals.

3.4. Ion Battery Applications

The graphene sheets (single and multilayers) were considered as anodic electrodes for the boron-ion batteries with the half-cell reactions taking place at the cathode and anode shown in Equations (4)–(7). Equation (8) also shows the overall cell reaction.



where B/B³⁺ is the boron atom/ion and “sheet” is the monolayer graphene sheet (MG), bilayer graphene sheet (BG), trilayer graphene sheet (TG), and tetralayer graphene sheet (TTG). The cell voltage (V_{cell}) and the cell energy are computed according to Equations (2) and (3).

As depicted in Figure 5, the adsorption energies of the boron atom(s) and/or ion(s) with the graphene sheets increased negatively as the number of the layers increased, with the boron ion (B³⁺) adsorption being more negative than the atomic counterparts. The monolayer graphene sheet (B³⁺/B@MG) has the least negative adsorption energy, while the tetralayer graphene sheet (B³⁺/B@TTG) showed the highest negative adsorption energy. The complexes with more negative adsorption energies express more favorable and deeper van der Waals interactions [65,77]. Table 2 shows the overall cell energies (ΔE_{cell}) and the corresponding voltages of the cells. The cells' energy increases with an increasing number of graphene sheets. However, for the intercalation of two atoms/ions of boron, the overall cell adsorption energy is higher. This can be attributed to the increased weak interactions between the graphene sheets and the two boron ions, which still permit free movement of the boron ions within the graphene layers during the charging and discharging processes.

Table 2. The overall cell energy change (ΔE_{cell}) and the cell voltages of the graphene sheet(s).

	ΔE_{cell} (kcal/mol)	V_{cell} (Volts)
B ³⁺ /B@MG	1.513	13.7
B ³⁺ /B@BG	1.701	15.4
B ³⁺ /B@TG	1.742	15.8
B ³⁺ /B@TTG_asym	1.815	16.5
B ³⁺ /B@TTG_sym	1.786	16.2
2B ³⁺ /2B@TG	2.723	12.4
2B ³⁺ /2B@TTG	2.959	13.4

Moreover, compared to sodium and lithium-ion batteries (SIBs and LIBs) [1] and other battery materials reported (Table 3), the voltages obtained here are significantly improved. The B³⁺/B@TTG showed the highest cell voltage of 16.5 V, which indicates that in addition to the complexes being efficient alternatives for the anodic electrode of boron-ion batteries, increasing the number of the graphene layers also improved the electrochemical performance of the storage system. Generally, the boron-graphene sheets have shown excellent voltage outputs, hinting at their suitability as anodic material(s) for enhancing the energy storage performance of boron-ion batteries (BIBs) if extensively studied.

Table 3. Comparison of the present results with those reported in the literature.

S/N	Support(s)	Dopant(s)	Cell Voltage(s)	Ref.
1	Boron nitride sheet	Li/Li ⁺ , Be/Be ²⁺ , Na/Na ⁺ , Mg/Mg ²⁺ , and polypyrrole	Li-ion = 2.06 V Na-ion = 1.37 V Be-ion = 6.60 V Mg-ion = 3.82 V	[1]
2	Boron nanorod	Li/Li ⁺	Li-ion = 2.00 V	[78]
3	Magnesium polymorphs	Na/Na ⁺	Na-ion = 1.5 V	[79]
4	Inorganic boron nitride nanocluster	Na/Na ⁺ , F ⁻ , Cl ⁻ , and Br ⁻	Na-ion = 3.39 V	[80]
5	Boron nitride nanosheet	Na/Na ⁺ , P, and Al	Na-ion = 2.31 V	[12]
6	Hexagonal boron phosphide	Li/Li ⁺ , Na/Na ⁺ , K/K ⁺	Li-ion = 1.37 V Na-ion = 0.97 V K-ion = 0.93 V	[81]
7	Aluminum/boron phosphide nanocluster	Na/Na ⁺ , F ⁻ , Cl ⁻ , and Br ⁻	Na/F@B ₁₂ P ₁₂ = 4.5 V Na/Cl@B ₁₂ P ₁₂ = 3.47 V Na/Br@B ₁₂ P ₁₂ = 3.5 V Na/F@Al ₁₂ P ₁₂ = 3.5 V Na/Cl@Al ₁₂ P ₁₂ = 3.22 V Na/Br@Al ₁₂ P ₁₂ = 3.20 V	[82]
8	Phosphorene	Mg/Mg ²⁺	Mg-ion = 0.833 V	[83]
9	Graphene-like MoS ₂ cathode and ultrasmall Mg nanoparticles	Mg/Mg ²⁺	Mg-ion = 1.8 V	[84]
10	B ₄₀ fullerenes	Mg/Mg ²⁺ , F ⁻ , Cl ⁻ , and Br ⁻	Mg-ion = 8.8 V	[85]
11	Multilayer graphene sheet	B/B ³⁺	B-ion = 16.5 V	Present study

4. Conclusions

We have studied the high-energy-density anodic compartment for boron-ion batteries as an alternative to lithium-ion and sodium-ion batteries using the first-principles calculations within the framework of Density Functional Theory. We investigated the electrochemical performance of the boron ion(s) on the monolayer, bilayer, trilayer, and tetralayer graphene sheet electrodes. Significant decreases in the HOMO–LUMO energy gap from -5.085 eV to -2.242 eV for B³⁺@MG and from -20.08 eV to -19.84 eV for 2B³⁺@TTG were recorded. The predominant interaction force for the graphene layers was van der Waals, as predicted by the reduced density gradient isosurface analyses, with the B³⁺@TTG_{asym} and B³⁺@TTG_{sym} configurations showing the most favorable interactions.

Furthermore, the electrochemical cell voltages obtained with the single-layer (B³⁺/B@MG) and/or multilayer (B³⁺/B@BG, B³⁺/B@TG, and B³⁺/B@TTG) graphene sheets were significantly improved, with B³⁺/B@MG (13.7 V) showing the least voltage. On the contrary, B³⁺/B@TTG (16.5 V) showed the highest voltage. The results revealed that increasing the number of graphene layers improves the electrochemical performance of the anodic electrode of the boron-ion battery. Therefore, the number of layers or the thickness of the graphene nanosheets is another effective parameter to tune the anode performance for boron-ion batteries. This might suggest an additional dimension to further engineer the graphene anode performance by increasing the number of graphene layers. Our theoretical investigations demonstrate the suitability of the graphene-based anodic electrodes for boron-ion batteries when extensively investigated for large-scale application as a highly efficient energy storage substitute for lithium- and sodium-based ion batteries, which could be beneficial to the material design of ion batteries.

Supplementary Materials: The following supporting information can be downloaded at: <https://www.mdpi.com/article/10.3390/nano12081280/s1>, Figure S1: Optimized structures of (a) and (b) 2B@TG (side and topviews), (c) and (d) 2B@TG (side and topviews), (e) and (f) 2B³⁺@TTG (side and topviews), (g) and (h) 2B³⁺@TTG (side and topviews); Figure S2: Molecular Orbital HOMO (Lower) and LUMO (upper) of (a) Monolayer Graphene Sheet (MG), (b) B@MG, (c) B³⁺@MG; Figure S3: Molecular Orbital HOMO (Lower) and LUMO (upper) of (a) Bilayer Graphene Sheet (BG) (b) B@BG, (c) B³⁺@BG; Figure S4: Molecular Orbital HOMO (Lower) and LUMO (upper) of (a) Trilayer Graphene Sheet (TG), (b) B@TG, (c) B³⁺@TG; Figure S5: Molecular Orbital HOMO (Lower) and LUMO (upper) of (a) 2B@TG and (b) 2B³⁺@TG; Figure S6: Electrostatic potential (ESP) map of (a) B³⁺@MG, (b) B³⁺@BG, (c) B³⁺@TG, (d) B³⁺@TTG_sym and (e) B³⁺@TTG_asym; Figure S7: Electrostatic potential (ESP) (a) 2B³⁺@TG and (b) 2B³⁺@TTG; Figure S8: The reduced density gradient (RDG) isosurfaces analyses of (a), (b) and (c) 2B³⁺@TG (complex and RDG), and (d), (e) and (f) 2B³⁺@TTG (complex and RDG). Where blue regions correspond to strong hydrogen bonds; red regions indicate strong steric effects, whereas green regions describe strong van der Waals interactions; Figure S9: Partial density of states (PDOS) plots (a) B@MG (b) B@BG and (c) B@TG; Figure S10: Partial density of states (PDOS) plots (a) 2B³⁺@TG (b) 2B³⁺@TTG (c) B@TG_sym and (d) 2B@TTG; Figure S11: Partial density of states (PDOS) plots of (a) B³⁺@MG (b) B³⁺@BG and (c) B³⁺@TG; Figure S12: Partial density of states (PDOS) plots of (a) B³⁺@TTG_sym (b) B³⁺@TTG_asym (c) B@TTG_sym and (d) B@TTG_asym; Figure S13: Natural bond orbital charges of (a) B³⁺@MG, (b) B³⁺@BG and (c) B³⁺@TG, (d) B³⁺@TTG_sym and (e) B³⁺@TTG_asym; Figure S14: Natural bond orbital charges of (a) 2B³⁺@TG and (b) 2B³⁺@TTG; Table S1: Electronic properties.

Author Contributions: Conceptualization, I.A. and Q.P.; methodology, A.A.A.-S.; software, A.A.A.-S. and Q.P.; validation, K.A., A.A.A.-S. and Q.P.; investigation, M.U., C.C.N. and M.H.; resources, I.A., A.A.A.-S. and Q.P.; writing—original draft preparation, M.U., C.C.N., and M.H.; writing—review and editing, I.A. and Q.P.; supervision, I.A. and Q.P.; project administration, K.A.; funding acquisition, Q.P. All authors have read and agreed to the published version of the manuscript.

Funding: The APC was funded by the Deanship of Scientific Research (DSR) at King Fahd University of Petroleum and Minerals (KFUPM) through project no. DF201020.

Institutional Review Board Statement: Not applicable.

Informed Consent Statement: Not applicable.

Data Availability Statement: The raw/processed data required to reproduce these findings cannot be shared at this time due to time limitations and will be made available by the corresponding author upon request.

Acknowledgments: For computing resources, we would like to acknowledge the ITC unit of the King Fahd University of Petroleum and Minerals (KFUPM) for providing access to the HPC computer resources.

Conflicts of Interest: The authors declare no conflict of interest.

Abbreviations

RDG	Reduced density gradient
MG	Monolayer graphene sheets
BG	Bilayer graphene sheets
TG	Trilayer graphene sheets
TTG	Tetralayer graphene sheets
B ³⁺ @MG	Absorbed boron ion on monolayer graphitic sheets
B@MG	Absorbed boron atom on monolayer graphitic sheets
B ³⁺ @BG	Intercalated boron ion in bilayer graphitic sheets
B@BG	Intercalated boron atom in bilayer graphitic sheets

B ³⁺ @TG	Intercalated boron ion in trilayer graphitic sheets
B@TG	Intercalated boron atom in trilayer graphitic sheets
2B ³⁺ @TG	Two intercalated boron ions in trilayer graphitic sheets
2B@TG	Two intercalated boron atoms in trilayer graphitic sheets
B ³⁺ @TTG	Intercalated boron ion in tetralayer graphitic sheets (in symmetry to the sheets)
B@TTG	Intercalated boron atom in tetralayer graphitic sheets (in symmetry to the sheets)
B ³⁺ @TTG	Intercalated boron ion in tetralayer graphitic sheets (in asymmetry to the sheets)
B@TTG	Intercalated boron atom in tetralayer graphitic sheets (in asymmetry to the sheets)
2B ³⁺ @TTG	Two intercalated boron ions in tetralayer graphitic sheets
2B@TTG	Two intercalated boron atoms in tetralayer graphitic sheets
HOMO	Highest occupied molecular orbital
LUMO	Lowest occupied molecular orbital
DFT	Density Functional Theory
PBE	Perdew–Burke–Ernzerhof
GGA	Generalized gradient approximation
E _{ad}	Adsorption energies
E _{Complex}	Energy of the complex (adsorbate and substrate)
E _{adsorbate}	Energy of the boron atom (ionic or neutral)
E _{Substrate}	Energy of the graphene sheets
RDG	Reduced density gradient
SIBs	Sodium-ion batteries
LIBs	Lithium-ion batteries
BIBs	Boron-ion batteries
PDOS	Projected density of states
DOS	Density of states
α-layer	The graphene layer directly beneath the intercalated boron atom/ion
β-layer	The graphene layer directly above the intercalated boron atom/ion
AA	Similar graphene layer stacking for bilayer
AB	Different graphene layer stacking for bilayer
ABA	Alternated graphene layer stacking for trilayer
AAB	Random graphene layer stacking for trilayer
ABAB	Alternated graphene layer stacking for tetralayer
AABA	Random graphene layer stacking for tetralayer
AABB	Regular graphene layer stacking for tetralayer

References

- Nnadike, C.C.; Abdulazeez, I.; Haroon, M.; Peng, Q.; Jalilov, A.; Al-Saadi, A. Impact of Polypyrrole Functionalization on the Anodic Performance of Boron Nitride Nanosheets: Insights from First-Principles Calculations. *Front. Chem.* **2021**, *9*, 274. [[CrossRef](#)] [[PubMed](#)]
- Chen, S.; Feng, F.; Che, H.; Yin, Y.; Ma, Z.-F. High Performance Solid-State Sodium Batteries Enabled by Boron Contained 3D Composite Polymer Electrolyte. *Chem. Eng. J.* **2021**, *406*, 126736. [[CrossRef](#)]
- Armand, M.; Tarascon, J.-M. Building Better Batteries. *Nature* **2008**, *451*, 652–657. [[CrossRef](#)] [[PubMed](#)]
- Prosini, P.P.; Cento, C.; Carewska, M.; Masci, A. Electrochemical Performance of Li-Ion Batteries Assembled with Water-Processable Electrodes. *Solid State Ion.* **2015**, *274*, 34–39. [[CrossRef](#)]
- Johannes, M.D.; Swider-Lyons, K.; Love, C.T. Oxygen Character in the Density of States as an Indicator of the Stability of Li-Ion Battery Cathode Materials. *Solid State Ion.* **2016**, *286*, 83–89. [[CrossRef](#)]
- Kino, K.; Yonemura, M.; Ishikawa, Y.; Kamiyama, T. Two-Dimensional Imaging of Charge/Discharge by Bragg Edge Analysis of Electrode Materials for Pulsed Neutron-Beam Transmission Spectra of a Li-Ion Battery. *Solid State Ion.* **2016**, *288*, 257–261. [[CrossRef](#)]
- Nitta, N.; Wu, F.; Lee, J.T.; Yushin, G. Li-Ion Battery Materials: Present and Future. *Mater. Today* **2015**, *18*, 252–264. [[CrossRef](#)]
- Youn, Y.; Gao, B.; Kamiyama, A.; Kubota, K.; Komaba, S.; Tateyama, Y. Nanometer-Size Na Cluster Formation in Micropore of Hard Carbon as Origin of Higher-Capacity Na-Ion Battery. *Npj Comput. Mater.* **2021**, *7*, 48. [[CrossRef](#)]
- Naumov, A.V.; Naumova, M.A. Modern State of the World Lithium Market. *Russ. J. Non-Ferrous Met.* **2010**, *51*, 324–330. [[CrossRef](#)]
- Grosjean, C.; Miranda, P.H.; Perrin, M.; Poggi, P. Assessment of World Lithium Resources and Consequences of Their Geographic Distribution on the Expected Development of the Electric Vehicle Industry. *Renew. Sustain. Energy Rev.* **2012**, *16*, 1735–1744. [[CrossRef](#)]
- Martin, G.; Rentsch, L.; Höck, M.; Bertau, M. Lithium Market Research—Global Supply, Future Demand and Price Development. *Energy Storage Mater.* **2017**, *6*, 171–179. [[CrossRef](#)]

12. Hosseinian, A.; Soleimani-amiri, S.; Arshadi, S.; Vessally, E.; Edjlali, L. Boosting the Adsorption Performance of BN Nanosheet as an Anode of Na-Ion Batteries: DFT Studies. *Phys. Lett. A* **2017**, *381*, 2010–2015. [[CrossRef](#)]
13. Barker, J.; Saidi, M.Y.; Swoyer, J.L. A Sodium-Ion Cell Based on the Fluorophosphate Compound NaVPO[Sub 4]F. *Electrochem. Solid-State Lett.* **2003**, *6*, A1. [[CrossRef](#)]
14. Er, D.; Li, J.; Naguib, M.; Gogotsi, Y.; Shenoy, B.V. Ti3C2 MXene as a High Capacity Electrode Material for Metal (Li, Na, K, Ca) Ion Batteries. *ACS Appl. Mater. Interfaces* **2014**, *6*, 11173–11179. [[CrossRef](#)]
15. Palomares, V.; Serras, P.; Villaluenga, I.; Hueso, K.B.; Carretero-González, J.; Rojo, T. Na-Ion Batteries, Recent Advances and Present Challenges to Become Low Cost Energy Storage Systems. *Energy Environ. Sci.* **2012**, *5*, 5884–5901. [[CrossRef](#)]
16. Yabuuchi, N.; Kubota, K.; Dahbi, M.; Komaba, S. Research Development on Sodium-Ion Batteries. *Chem. Rev.* **2014**, *114*, 11636–11682. [[CrossRef](#)]
17. Landi, B.J.; Ganter, M.J.; Cress, C.D.; DiLeo, R.A.; Raffaele, R.P. Carbon Nanotubes for Lithium Ion Batteries. *Energy Environ. Sci.* **2009**, *2*, 638–654. [[CrossRef](#)]
18. Jeong, M.; Ahn, S.; Yokoshima, T.; Nara, H.; Momma, T.; Osaka, T. New Approach for Enhancing Electrical Conductivity of Electrodeposited Si-Based Anode Material for Li Secondary Batteries: Self-Incorporation of Nano Cu Metal in Si–O–C Composite. *Nano Energy* **2016**, *28*, 51–62. [[CrossRef](#)]
19. Jiang, Q.; Zhang, Z.; Yin, S.; Guo, Z.; Wang, S.; Feng, C. Biomass Carbon Micro/Nano-Structures Derived from Ramie Fibers and Corncoals as Anode Materials for Lithium-Ion and Sodium-Ion Batteries. *Appl. Surf. Sci.* **2016**, *379*, 73–82. [[CrossRef](#)]
20. Golberg, D.; Bando, Y.; Huang, Y.; Terao, T.; Mitome, M.; Tang, C.; Zhi, C. Boron Nitride Nanotubes and Nanosheets. *ACS Nano* **2010**, *4*, 2979–2993. [[CrossRef](#)]
21. Peyghan, A.A.; Noei, M.; Yourdkhani, S. Al-Doped Graphene-like BN Nanosheet as a Sensor for Para-Nitrophenol: DFT Study. *Superlattices Microstruct.* **2013**, *59*, 115–122. [[CrossRef](#)]
22. Shao, D.; Tang, D.; Yang, J.; Li, Y.; Zhang, L. Nano-Structured Composite of Si/(S-Doped-Carbon Nanowire Network) as Anode Material for Lithium-Ion Batteries. *J. Power Sources* **2015**, *297*, 344–350. [[CrossRef](#)]
23. Gurung, A.; Naderi, R.; Vaagensmith, B.; Varnekar, G.; Zhou, Z.; Elbohy, H.; Qiao, Q. Tin Selenide—Multi-Walled Carbon Nanotubes Hybrid Anodes for High Performance Lithium-Ion Batteries. *Electrochim. Acta* **2016**, *211*, 720–725. [[CrossRef](#)]
24. Chen, B.; Chu, S.; Cai, R.; Wei, S.; Hu, R.; Zhou, J. First-Principles Simulations of Lithiation–Deformation Behavior in Silicon Nanotube Electrodes. *Comput. Mater. Sci.* **2016**, *123*, 44–51. [[CrossRef](#)]
25. Peyghan, A.A.; Noei, M. A Theoretical Study of Lithium-Intercalated Pristine and Doped Carbon Nanocones. *J. Mex. Chem. Soc.* **2014**, *58*, 46–51.
26. Lee, S.W.; Yabuuchi, N.; Gallant, B.M.; Chen, S.; Kim, B.-S.; Hammond, P.T.; Shao-Horn, Y. High-Power Lithium Batteries from Functionalized Carbon-Nanotube Electrodes. *Nat. Nanotechnol.* **2010**, *5*, 531–537. [[CrossRef](#)] [[PubMed](#)]
27. Liu, Y.; Artyukhov, V.I.; Liu, M.; Harutyunyan, A.R.; Yakobson, I.B. Feasibility of Lithium Storage on Graphene and Its Derivatives. *J. Phys. Chem. Lett.* **2013**, *4*, 1737–1742. [[CrossRef](#)]
28. Qie, L.; Chen, W.-M.; Wang, Z.-H.; Shao, Q.-G.; Li, X.; Yuan, L.-X.; Hu, X.-L.; Zhang, W.-X.; Huang, Y.-H. Nitrogen-Doped Porous Carbon Nanofiber Webs as Anodes for Lithium Ion Batteries with a Superhigh Capacity and Rate Capability. *Adv. Mater.* **2012**, *24*, 2047–2050. [[CrossRef](#)]
29. Wu, Z.-S.; Ren, W.; Xu, L.; Li, F.; Cheng, H.-M. Doped Graphene Sheets As Anode Materials with Superhigh Rate and Large Capacity for Lithium Ion Batteries. *ACS Nano* **2011**, *5*, 5463–5471. [[CrossRef](#)]
30. Hardikar, R.P.; Das, D.; Han, S.S.; Lee, K.-R.; Singh, A.K. Boron Doped Defective Graphene as a Potential Anode Material for Li-Ion Batteries. *Phys. Chem. Chem. Phys.* **2014**, *16*, 16502–16508. [[CrossRef](#)]
31. Yu, Y.-X. Can All Nitrogen-Doped Defects Improve the Performance of Graphene Anode Materials for Lithium-Ion Batteries? *Phys. Chem. Chem. Phys.* **2013**, *15*, 16819–16827. [[CrossRef](#)]
32. Chen, C.; Wang, Z.; Zhang, B.; Miao, L.; Cai, J.; Peng, L.; Huang, Y.; Jiang, J.; Huang, Y.; Zhang, L.; et al. Nitrogen-Rich Hard Carbon as a Highly Durable Anode for High-Power Potassium-Ion Batteries. *Energy Storage Mater.* **2017**, *8*, 161–168. [[CrossRef](#)]
33. Xu, D.; Chen, C.; Xie, J.; Zhang, B.; Miao, L.; Cai, J.; Huang, Y.; Zhang, L. A Hierarchical N/S-Codoped Carbon Anode Fabricated Facilely from Cellulose/Polyaniline Microspheres for High-Performance Sodium-Ion Batteries. *Adv. Energy Mater.* **2016**, *6*, 1501929. [[CrossRef](#)]
34. Cao, Q.; Geng, X.; Wang, H.; Wang, P.; Liu, A.; Lan, Y.; Peng, Q. Crystals A Review of Current Development of Graphene Mechanics. *Crystals* **2018**, *8*, 357. [[CrossRef](#)]
35. Peng, Q.; Han, L.; Lian, J.; Wen, X.; Liu, S.; Chen, Z.; Koratkar, N.; De, S. Mechanical Degradation of Graphene by Epoxidation: Insights from First-Principles Calculations. *Phys. Chem. Chem. Phys.* **1948**, *17*, 19484. [[CrossRef](#)]
36. Wang, L.; Jin, J.; Yang, P.; Zong, Y.; Peng, Q. Graphene Adhesion Mechanics on Iron Substrates: Insight from Molecular Dynamic Simulations. *Crystals* **2019**, *9*, 579. [[CrossRef](#)]
37. Chen, Y.; Wang, S.; Xie, L.; Zhu, P.; Li, R.; Peng, Q. Grain Size and Hydroxyl-Coverage Dependent Tribology of Polycrystalline Graphene. *Nanotechnology* **2019**, *30*, 385701. [[CrossRef](#)]
38. Chen, H.; Chen, Z.; Yang, H.; Wen, L.; Yi, Z.; Zhou, Z.; Dai, B.; Zhang, J.; Wu, X.; Wu, P. Multi-Mode Surface Plasmon Resonance Absorber Based on Dart-Type Single-Layer Graphene. *RSC Adv.* **2022**, *12*, 7821–7829. [[CrossRef](#)]

39. Zhang, Z.; Cai, R.; Long, F.; Wang, J. Development and Application of Tetrabromobisphenol A Imprinted Electrochemical Sensor Based on Graphene/Carbon Nanotubes Three-Dimensional Nanocomposites Modified Carbon Electrode. *Talanta* **2015**, *134*, 435–442. [[CrossRef](#)]
40. Tang, N.; Li, Y.; Chen, F.; Han, Z. In Situ Fabrication of a Direct Z-Scheme Photocatalyst by Immobilizing CdS Quantum Dots in the Channels of Graphene-Hybridized and Supported Mesoporous Titanium Nanocrystals for High Photocatalytic Performance under Visible Light. *RSC Adv.* **2018**, *8*, 42233–42245. [[CrossRef](#)]
41. Xiao, L.; Youji, L.; Feitai, C.; Peng, X.; Ming, L. Facile Synthesis of Mesoporous Titanium Dioxide Doped by Ag-Coated Graphene with Enhanced Visible-Light Photocatalytic Performance for Methylene Blue Degradation. *RSC Adv.* **2017**, *7*, 25314–25324. [[CrossRef](#)]
42. Peng, Q.; Chen, X.-J.; Ji, W.; De, S. Chemically Tuning Mechanics of Graphene by BN. *Adv. Eng. Mater.* **2013**, *15*, 718–727. [[CrossRef](#)]
43. Peng, Q.; Liang, C.; Ji, W.; De, S. A theoretical analysis of the effect of the hydrogenation of graphene to graphane on its mechanical properties. *Phys. Chem. Chem. Phys.* **2013**, *15*, 2003–2011. [[CrossRef](#)]
44. Hou, J.; Deng, B.; Zhu, H.; Lan, Y.; Shi, Y.; De, S.; Liu, L.; Chakraborty, P.; Gao, F.; Peng, Q. Magic Auxeticity Angle of Graphene. *Carbon* **2019**, *149*, 350–354. [[CrossRef](#)]
45. Deng, B.; Hou, J.; Zhu, H.; Liu, S.; Liu, E.; Shi, Y.; Peng, Q. The normal-auxeticity mechanical phase transition in graphene. *2D Mater.* **2017**, *4*, 021020. [[CrossRef](#)]
46. Wang, W.; Peng, Q.; Dai, Y.; Qian, Z.; Liu, S. Distinctive Nanofriction of Graphene Coated Copper Foil. *Comput. Mater. Sci.* **2016**, *117*, 406–411. [[CrossRef](#)]
47. Alahmed, I.I.; Altanany, S.M.; Abdulazeez, I.; Shoaib, H.; Alsayoud, A.Q.; About, A.; Peng, Q.; Sa, A.A. The Crack Angle of 60 ° Is the Most Vulnerable Crack Front in Graphene According to MD Simulations. *Crystals* **2021**, *11*, 1355. [[CrossRef](#)]
48. Shoaib, H.; Peng, Q.; Alsayoud, A.Q.; Sa, A.Q.A. Atomic Insights into Fracture Characteristics of Twisted Tri-Layer Graphene. *Crystals* **2021**, *11*, 1202. [[CrossRef](#)]
49. Peng, Q.; Peng, S.; Cao, Q. Ultrahigh Ballistic Resistance of Twisted Bilayer Graphene. *Crystals* **2021**, *11*, 206. [[CrossRef](#)]
50. Allen, M.J.; Tung, V.C.; Kaner, R.B. Honeycomb Carbon: A Review of Graphene. *Chem. Rev.* **2010**, *110*, 132–145. [[CrossRef](#)]
51. Lian, P.; Zhu, X.; Liang, S.; Li, Z.; Yang, W.; Wang, H. Large Reversible Capacity of High Quality Graphene Sheets as an Anode Material for Lithium-Ion Batteries. *Electrochim. Acta* **2010**, *55*, 3909–3914. [[CrossRef](#)]
52. Yang, S.; Gong, Y.; Liu, Z.; Zhan, L.; Hashim, D.P.; Ma, L.; Vajtai, R.; Ajayan, P.M. Bottom-up Approach toward Single-Crystalline VO₂-Graphene Ribbons as Cathodes for Ultrafast Lithium Storage. *Nano Lett.* **2013**, *13*, 1596–1601. [[CrossRef](#)] [[PubMed](#)]
53. Paek, S.-M.; Yoo, E.; Honma, I. Enhanced Cyclic Performance and Lithium Storage Capacity of SnO₂/Graphene Nanoporous Electrodes with Three-Dimensionally Delaminated Flexible Structure. *Nano Lett.* **2009**, *9*, 72–75. [[CrossRef](#)] [[PubMed](#)]
54. Zhou, D.; Cui, Y.; Han, B. Graphene-Based Hybrid Materials and Their Applications in Energy Storage and Conversion. *Chin. Sci. Bull.* **2012**, *57*, 2983–2994. [[CrossRef](#)]
55. Zhang, J.; Hu, Y.-S.; Tessonier, J.-P.; Weinberg, G.; Maier, J.; Schlögl, R.; Su, D.S. CNFs@CNTs: Superior Carbon for Electrochemical Energy Storage. *Adv. Mater.* **2008**, *20*, 1450–1455. [[CrossRef](#)]
56. Yang, S.; Huo, J.; Song, H.; Chen, X. A Comparative Study of Electrochemical Properties of Two Kinds of Carbon Nanotubes as Anode Materials for Lithium Ion Batteries. *Electrochim. Acta* **2008**, *53*, 2238–2244. [[CrossRef](#)]
57. Gerouki, A.; Goldner, M.A.; Goldner, R.B.; Haas, T.E.; Liu, T.Y.; Slaven, S. Density of States Calculations of Small Diameter Single Graphene Sheets. *J. Electrochem. Soc.* **1996**, *143*, L262–L263. [[CrossRef](#)]
58. Ling, C.; Mizuno, F. Boron-Doped Graphene as a Promising Anode for Na-Ion Batteries. *Phys. Chem. Chem. Phys.* **2014**, *16*, 10419–10424. [[CrossRef](#)]
59. Farsi, L.; Deskins, N.A. First principles analysis of surface dependent segregation in bimetallic alloys. *Phys. Chem. Chem. Phys.* **2019**, *21*, 23626–23637. [[CrossRef](#)]
60. Haas, P.; Tran, F.; Blaha, P. Calculation of the Lattice Constant of Solids with Semilocal Functionals. *Phys. Rev. B* **2009**, *79*, 85104. [[CrossRef](#)]
61. Janthon, P.; Luo, S.; Kozlov, S.M.; Vin, F.; Limtrakul, J.; Truhlar, D.G.; Illas, F. Bulk Properties of Transition Metals: A Challenge for the Design of Universal Density Functionals. *J. Chem. Theory Comput.* **2014**, *10*, 3832–3839. [[CrossRef](#)] [[PubMed](#)]
62. Perdew, J.P.; Burke, K.; Ernzerhof, M. Generalized Gradient Approximation Made Simple. *Phys. Rev. Lett.* **1996**, *77*, 3865. [[CrossRef](#)] [[PubMed](#)]
63. Lieb, E.H.; Oxford, S. Improved Lower Bound on the Indirect Coulomb Energy. *Int. J. Quantum Chem.* **1981**, *19*, 427–439. [[CrossRef](#)]
64. Abdulazeez, I.; Khaled, M.; Al-Saadi, A.A. Impact of Electron-Withdrawing and Electron-Donating Substituents on the Corrosion Inhibitive Properties of Benzimidazole Derivatives: A Quantum Chemical Study. *J. Mol. Struct.* **2019**, *1196*, 348–355. [[CrossRef](#)]
65. Umar, M.; Nnadike, C.C.; Abdulazeez, I.; Alhooshani, K.; Al-Saadi, A.A. Nitrogen-Enhanced Charge Transfer Efficacy on the Carbon Sheet: A Theoretical Insight Into the Adsorption of Anionic Dyes. *Arab. J. Sci. Eng.* **2021**. [[CrossRef](#)]
66. Li, M.-Y.; Zhao, Y.-X.; Han, Y.-B.; Yuan, K.; Nagase, S.; Ehara, M.; Zhao, X. Theoretical Investigation of the Key Roles in Fullerene-Formation Mechanisms: Enantiomer and Enthalpy. *ACS Appl. Nano Mater.* **2020**, *3*, 547–554. [[CrossRef](#)]

67. Pounraj, P.; Ramasamy, P.; Senthil Pandian, M. The Influence of π -Linkers Configuration on Properties of 10-Hexylphenoxazine Donor-Based Sensitizer for Dye-Sensitized Solar Cell Application—Theoretical Approach. *J. Mol. Graph. Model.* **2021**, *102*, 107779. [[CrossRef](#)]
68. Peng, Q.; Wang, G.; Liu, G.-R.; De, S. Van Der Waals Density Functional Theory VdW-DFq for Semihard Materials. *Crystals* **2019**, *9*, 243. [[CrossRef](#)]
69. Umar, M.; Abdulazeez, I.; Tanimu, A.; Ganiyu, S.A.; Alhooshani, K. Modification of ZSM-5 Mesoporosity and Application as Catalyst Support in Hydrodesulfurization of Dibenzothiophene: Experimental and DFT Studies. *J. Environ. Chem. Eng.* **2021**, *9*, 106738. [[CrossRef](#)]
70. O'Boyle, N.M.; Tenderholt, A.L.; Langner, K.M. Cclib: A Library for Package-Independent Computational Chemistry Algorithms. *J. Comput. Chem.* **2008**, *29*, 839–845. [[CrossRef](#)]
71. Wu, X.; Zhang, Z.; Soleymanabadi, H. Substituent Effect on the Cell Voltage of Nanographene Based Li-Ion Batteries: A DFT Study. *Solid State Commun.* **2020**, *306*, 113770. [[CrossRef](#)]
72. Bibi, S.; Bilal, S.; Ali Shah, A.-H.; Ullah, H. Systematic Analysis of Poly(o-Aminophenol) Humidity Sensors. *ACS Omega* **2017**, *2*, 6380–6390. [[CrossRef](#)] [[PubMed](#)]
73. Wang, G.; Yu, M.; Feng, X. Carbon Materials for Ion-Intercalation Involved Rechargeable Battery Technologies. *Chem. Soc. Rev.* **2020**, *50*, 2388–2443. [[CrossRef](#)] [[PubMed](#)]
74. Bader, R.F.W. *A Quantum Theory*; Clarendon Press: Oxford, UK, 1994.
75. Abdelnaby, M.M.; Cordova, K.E.; Abdulazeez, I.; Alloush, A.M.; Al-Maythaly, B.A.; Mankour, Y.; Alhooshani, K.; Saleh, T.A.; Charles, O.; Al Hamouz, S. Novel Porous Organic Polymer for the Concurrent and Selective Removal of Hydrogen Sulfide and Carbon Dioxide from Natural Gas Streams. *ACS Appl. Mater. Interfaces* **2020**, *12*, 47992. [[CrossRef](#)]
76. Zhang, C.; Derakhshandeh, M. CS₂ Adsorption on Pristine and Al-Doped Graphynes: A DFT Study. *Comput. Theor. Chem.* **2021**, *1204*, 113380. [[CrossRef](#)]
77. Nnadike, C.C.; Nada, A.; Abdulazeez, I.; Imam, M.R.; Janjua, M.R.S.A.; Al-Saadi, A.A. UV-Absorbing Benzamide-Based Dendrimer Precursors: Synthesis, Theoretical Calculation, and Spectroscopic Characterization. *New J. Chem.* **2022**, *46*, 75–85. [[CrossRef](#)]
78. Deng, C.; Lau, M.L.; Barkholtz, H.M.; Xu, H.; Parrish, R.; Xu, M.O.; Xu, T.; Liu, Y.; Wang, H.; Connell, J.G.; et al. Amorphous Boron Nanorod as an Anode Material for Lithium-Ion Batteries at Room Temperature. *Nanoscale* **2017**, *9*, 10757–10763. [[CrossRef](#)]
79. Nayak, D.; Ghosh, S.; Adyam, V. Thin Film Manganese Oxide Polymorphs as Anode for Sodium-Ion Batteries: An Electrochemical and DFT Based Study. *Mater. Chem. Phys.* **2018**, *217*, 82–89. [[CrossRef](#)]
80. Nejati, K.; Hosseinian, A.; Bekhradnia, A.; Vessally, E.; Edjlali, L. Na-Ion Batteries Based on the Inorganic BN Nanocluster Anodes: DFT Studies. *J. Mol. Graph. Model.* **2017**, *74*, 1–7. [[CrossRef](#)]
81. Ullah, S.; Denis, P.A.; Sato, F. Hexagonal Boron Phosphide as a Potential Anode Nominee for Alkali-Based Batteries: A Multi-Flavor DFT Study. *Appl. Surf. Sci.* **2019**, *471*, 134–141. [[CrossRef](#)]
82. Kosar, N.; Asgar, M.; Ayub, K.; Mahmood, T. Halides Encapsulation in Aluminum/Boron Phosphide Nanoclusters: An Effective Strategy for High Cell Voltage in Na-Ion Battery. *Mater. Sci. Semicond. Process.* **2019**, *97*, 71–79. [[CrossRef](#)]
83. Han, X.; Liu, C.; Sun, J.; Sendek, A.D.; Yang, W. Density Functional Theory Calculations for Evaluation of Phosphorene as a Potential Anode Material for Magnesium Batteries. *RSC Adv.* **2018**, *8*, 7196–7204. [[CrossRef](#)]
84. Liang, Y.; Feng, R.; Yang, S.; Ma, H.; Liang, J.; Chen, J. Rechargeable Mg Batteries with Graphene-like MoS₂ Cathode and Ultrasmall Mg Nanoparticle Anode. *Adv. Mater.* **2011**, *23*, 640–643. [[CrossRef](#)] [[PubMed](#)]
85. Shakerzadeh, E.; Kazemimoghadam, F. Magnesium of Bare and Halides Encapsulated B₄₀ Fullerenes for Their Potential Application as Promising Anode Materials for Mg-Ion Batteries. *Appl. Surf. Sci.* **2021**, *538*, 148060. [[CrossRef](#)]